Numerical modeling and analysis of the thermal behavior of NCM lithium-ion batteries subjected to very high C-rate discharge/charge operations

Ti Dong [a,b,c,d], Peng Peng [a,b,c], Fangming Jiang [a,b,c,*]

[a] *Guangzhou Institute of Energy Conversion, Chinese Academy of Sciences (CAS), Guangzhou 510640, China*
[b] *CAS Key Laboratory of Renewable Energy, Guangzhou 510640, China*
[c] *Guangdong Key Laboratory of New and Renewable Energy Research and Development, Guangzhou 510640, China*
[d] *University of Chinese Academy of Sciences, Beijing 100049, China*

A B S T R A C T

Lithium-ion batteries are easily overheated during discharge/charge operations with large current output/input. Traditional battery tests are difficult to pinpoint the internal thermal mechanism for an overheated battery. In this study, it is proposed a model to investigate the thermal behavior of the charge and discharge processes of lithium-ion battery with very high C-rate. The model combines an electrochemical-thermal (ECT) coupled module and a thermal abuse module. The whole successive process of the cell operation including charge/discharge, battery material exothermic reactions, and even thermal runaway within a cell, is fully described, by a single model. Predictions of individual LiNi$_x$Co$_y$Mn$_z$O$_2$ (NCM) lithium-ion cell high C-rate (up to 8C) discharge/charge processes compare well with experimental data. A detailed analysis is conducted to evaluate the influence of external heat release condition and charge/discharge C-rate on the thermal behavior of batteries during and after very high C-rate (>8C) charge/discharge operations. Results indicate: (1) the very large output/input current leads to the early-coming of cut-off voltage, terminating the discharge/charge operation; (2) compared with the very high C-rate charge operation, the discharge operation of the same C-rate is easier to cause battery overheat, leading to the occurrence of battery thermal runaway; (3) the high C-rate charge operation with cut-off voltage control fault is very dangerous as it can cause very fast heat generation and eventually possible thermal runaway; (4) favorable heat release condition or effective and active thermal control may be the key to the thermal control and restraining thermal runaway of lithium-ion batteries.

© 2017 Elsevier Ltd. All rights reserved.

1. Introduction

Lithium-ion batteries (LIBs) are common in a variety of energy storage applications. Batteries with LiNi$_x$Co$_y$Mn$_z$O$_2$ (NCM) or LiNi$_x$Co$_y$Al$_z$O$_2$ (NCA) cathode are widely used in electrical vehicles (EVs), such as BMW i3, Chevrolet Volt, Nissan Leaf, and Tesla Model S and Model 3. The frequent incidents including combustion and explosion of LIBs indicate that the safety issue persists to be one major challenge that prevents the large-scale commercialization of EVs. Overheat of battery in the discharge/charge process is one of the main causes for these incidents [1].

During high or very high C-rate charge/discharge processes, LIBs are more vulnerable to overheat because a large amount heat is generated in the cell at a very high rate; the overheat of battery may feed the subsequent abusive reactions of battery materials causing further overheat of the battery, which, in turn, may result in thermal runaway or even incidents like combustion and explosion [2]. The EVs applications of LIB require the battery to tolerate relatively high C-rate discharge/charge operations. Therefore, considerable research on the thermal behavior of LIBs during high or very high C-rate discharge/charge operations is a must.

Numerous publications dealing with the thermal behavior of LIBs during charge/discharge processes have appeared in the open literature. Quadir et al. [3] measured the overpotential and entropic heat generation and calculated the heat generation in a Li-ion cell during 1C-4C discharge processes. Drake et al. [4] measured the cell temperature and surface heat flux to determine the heat generation rate in batteries with high discharge rates, up to 9.6C. The detailed temperature distribution across the surface of a large format 20 Ah pouch cell was investigated over a wide ranges of

Nomenclature

List of symbols

A	side surface area of the electrode plate (m^2)
A_{sei}	SEI decomposition frequency factor (s^{-1})
A_{ne}	negative-solvent frequency factor (s^{-1})
A_{pe}	positive-solvent frequency factor (s^{-1})
A_e	electrolyte decomposition frequency factor (s^{-1})
A_s	side surface area of the electrode plate (m^2)
a_s	specific surface area (m^{-1})
c	Li$^+$ concentration (mol m^{-3})
c_{ele}	dimensionless concentration of electrolyte
c_{neg}	dimensionless amount of lithium within the carbon
c_p	specific heat capacity (J kg^{-1} K^{-1})
c_{sei}	dimensionless amount of lithium containing meta-stable species in the SEI
D	diffusion coefficient (m^2 s^{-1})
$E_{a,sei}$	SEI decomposition activation energy (J mol^{-1})
$E_{a,ne}$	negative-solvent activation energy (J mol^{-1})
$E_{a,pe}$	positive-solvent activation energy (J mol^{-1})
$E_{a,e}$	electrolyte decomposition activation energy (J mol^{-1})
F	Faraday's constant (C mol^{-1})
h	equivalent heat transfer coefficient (Wm^{-2} K^{-1})
H_{sei}	SEI-decomposition heat (J kg^{-1})
H_{ne}	negative-solvent reaction heat (J kg^{-1})
H_{pe}	positive-solvent reaction heat (J kg^{-1})
H_e	electrolyte decomposition heat (J kg^{-1})
I	current load (A)
i_o	exchange current density (A m^{-2})
j^{Li}	transfer current density (A m^{-3})
L	through-plane thickness of the battery
L_e	through-plane thickness of the electrode (m)
m_{sei}	reaction order for c_{sei}
$m_{ne,n}$	reaction order for c_{neg}
$m_{pe,p1}$	reaction order for a
$m_{pe,p2}$	reaction order for $(1-a)$
m_e	reaction order for c_e
p	Bruggeman factor
q	volumetric heat generation rate
q_c	contact resistance heat (W m^{-3})
q_{ele}	heat from electrolyte decomposition reaction (W m^{-3})
q_i	ionic ohmic heat (W m^{-3})
q_{ir}	heat from irreversible electrochemical reaction (W m^{-3})
q_{ne}	heat from reaction between negative active material and electrolyte (W m^{-3})
q_o	ohmic heat (W m^{-3})
q_{pe}	heat from reaction between positive active material and electrolyte (W m^{-3})
q_{re}	reversible entropic heat (W m^{-3})
q_{sei}	heat from the SEI decomposition reaction (W m^{-3})
Q_1	total heat generation rate form ECT model (W m^{-3})
Q_2	total heat generation from exothermic reactions of battery materials (W m^{-3})

r	radius of solid active particles (m)
R_c	the total lumped contact resistance (Ω m^2)
R_{sei}	SEI-decomposition reaction rate (s^{-1})
R_{ne}	negative-solvent reaction rate (s^{-1})
R_{pe}	positive-solvent reaction rate (s^{-1})
R_e	electrolyte decomposition reaction rate (s^{-1})
T	temperature (K)
T_{amb}	ambient temperature
T_{ref}	reference temperature (K)
T_{sur}	temperature at the cell surface (K)
t	time (s)
t_e	characteristic time
t_s	characteristic time
t_c	characteristic time
t_+^0	transference number of Li dissolved in the electrolyte
t_{sei}	dimensionless measure of SEI layer thickness that reflects the amount of lithium in the SEI
U	open-circuit potential (V)
V	cell voltage (V)
v	volume of numerical element interfacing separator and electrode (m^{-3})
W_c	volume-specific carbon content before abusive reactions (kg m^{-3})
W_p	volume-specific active material content in cathode before abusive reactions (kg m^{-3})
W_e	volume-specific electrolyte content before abusive reactions (kg m^{-3})

Greek symbols

α	degree of conversion
α_a	anodic transfer coefficient
α_c	cathodic transfer coefficient
ε	porosity
η	surface overpotential (V)
κ	ionic conductivity (S m^{-1})
λ	thermal conductivity (W m^{-1} K)
ρ	density (kg m^{-3})
σ	electronic conductivity (S m^{-1})
φ	electric potential (V)
δ	thickness of copper collector (m)

Subscripts/superscripts

0	initial value
e	electrolyte phase
eff	effective value
neg	negative electrode
pos	positive electrode
s	solid phase
sep	separator

ambient temperature and discharge/charge C-rate (0.5C-10C) [5]. The core temperature of a Li-ion cell was indirectly determined by integrating spatio-temporally the measured temperature field on the outside surface of the battery during 2C-10C discharge processes [6]. However, the thermal behavior of Li-ion batteries during higher C-rate (particularly >10C) operations, which probably causes battery destruction or even thermal runaway, is rarely studied.

Numerical models are also widely used to study the involved thermal behavior characteristics of batteries during charge/discharge operations of various C-rates. The established or employed

models can be classified as: electrochemical-thermal (ECT) coupling model [2,7–14], electro-thermal (ET) coupling model [15,16], equivalent circuit model (ECM) [10], and partially coupled model [17,18]. The simulated discharge/charge operations were mostly below 10C except the work by Cai and White [11], in which they modeled the 0.1C-20C discharge processes and found that the maximum cell temperature rise (70 °C) was harvested at the interruption time of 10C discharge operation when the cut-off voltage (3.0 V) was reached.

Super high C-rate (up to 50C or even 397C) discharge processes were explored with respect to batteries of special cathode materi-

als: synthesized $LiFe_{0.9}P_{0.95}O_{4-\delta}$ and nanoscale graphene-modified $LiFePO_4$ [19,20]. Nevertheless, no thermal analysis was conveyed in these studies, and the work reported in reference [19] was challenged for lacking heat generation analysis and its infeasibility for very high C-rate operations [21]. To date, for LIBs with normal electrode materials (common materials and micrometer-sized active material particles), few studies were conducted to investigate their thermal behaviors during discharge/charge operations of very high C-rate (particularly >8C).

Previous work studying the overheat of LIBs was mostly focused on constant power heating [22] or constant temperature heating such as oven tests [23–25]; in [14] and [17], overheat of battery was caused by the adiabatic thermal conditions while the discharge/charge C-rate was not higher than 1.5C. No published work explicitly addresses the thermal behavior of LIBs during a practical high or very high C-rate discharge/charge process, in which overheat of the battery is first caused by the ineffectiveness of the charge/discharge operations followed by the reaction heat resulted from the eventual abusive reactions of the battery materials.

In the present work, we combine the ECT module of battery charge/discharge process and the thermal module for abusive reactions of battery materials to study the thermal behavior of NMC batteries during and after very high C-rate (>8C) discharge/charge processes. Main attention is placed on the relation between the thermal behavior of the battery and the heat evolution inside the battery and the external heat release conditions. The conditions for triggering thermal runaway are also discussed in some detail. The obtained results may find use in the design of actual battery thermal management systems (BTMS).

2. Model description

The model consists of an electrochemical-thermal (ECT) coupling module [8] for battery charge/discharge processes and a thermal module [23] for battery material abusive reactions.

The cylinder-spiral 18650 battery is rolled up with a single layer cell. To study the thermal behavior of the 18650 battery during charge/discharge process, Fang et al. [13] and Lee et al. [26], for calculation purposes, approximated the cylinder-spiral structure to an unfolded single layer cell and they assumed a uniform current distribution over the entire electrode area. In fact, the multi transport and lithium generation/consumption processes in a cylindrical battery can be covered in their entirety by this long single layer cell [26]. In the present work, the cylinder-spiral battery is also approximated by a single layer cell. Fig. 1 illustrates the inner structure of the battery and schematically displays the principle of the charge/discharge operation.

2.1. Mathematic model

2.1.1. Electrochemical thermal model

The ECT model for NCM batteries is based on porous electrode and concentrated solution formulations [27,28]. The main assumptions made in this model are as follows: (1) Electrode active materials are considered to be spherical particles of uniform size. (2) Li^+ transport in the electrolyte relies on diffusion and migration and diffusion only in the solid active material particles. (3) Interfacial electrical and chemical equilibrium exist at the electrode/electrolyte interface. (4) Electrochemical reaction rates of Li^+ insertion and extraction processes are assumed to follow the Butler-Volmer equation. Table 1 summarizes the governing equations and boundary conditions of the ECT model.

The transport of the electric charges in the solid phase and solution phase is described by Eqs. (1) and (2), respectively. A constant current density related to the C-rate of the discharge/charge oper-
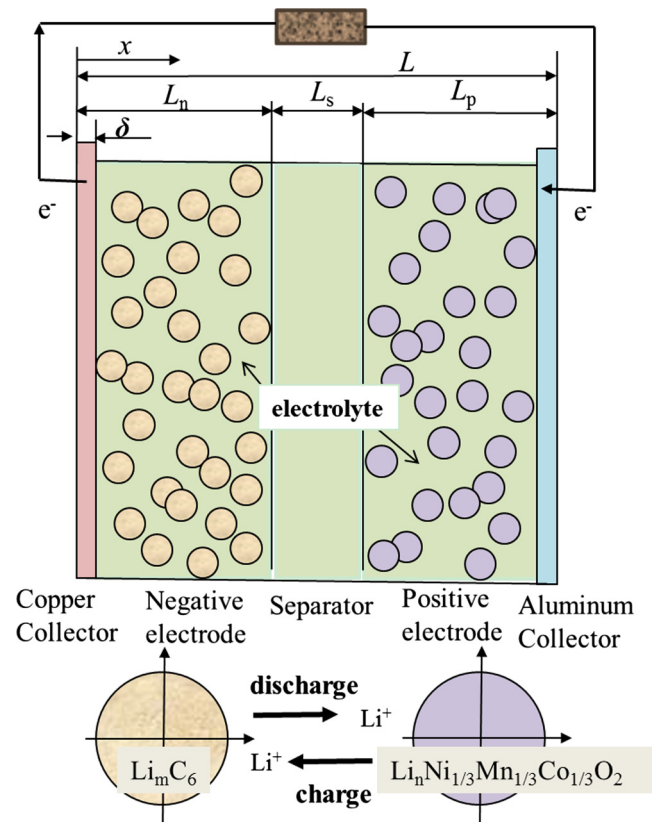

Fig. 1. Schematic of the Li-ion cell macroscopic model coupled with microscopic (*r*-direction) solid-diffusion submodel.

ation is imposed at the outer surface of the current collector for both anode and cathode side; zero-potential is set at the outer surface of anode current collector as the reference potential. For charge and discharge operations of the same C-rate, the imposed current density at the boundaries has the same magnitude, but takes opposite sign. The lithium-ion transport in the electrolyte follows Eq. (3); the lithium diffusion in the solid active materials is described by the Fick's second law as expressed by Eq. (4). The heat transport is governed by the energy conservation equation, Eq. (5), where Q_1 is the summation of all the heat generation/consumption terms including the irreversible electrochemical reaction heat, ohmic heat, ionic migration heat, reversible entropic heat and contact resistance heat during battery discharge/charge operations, and Q_2 represents the total heat generated due to the exothermic reactions of the battery materials, which will be further discussed in the next subsection in relation to the thermal abuse model. Eq. (5) contains the heat source/sink terms of the ECT module and battery material abusive reaction model both; therefore, the thermal behavior during the whole process that encompasses the (very) high-rate charge/discharge process and the possibly occurring thermal runaway can be described by the single governing equation, Eq. (5). During charge/discharge operations, when the cell temperature is lower than the critical value that can trigger the battery material abusive reactions, the Q_2 in Eq. (5) vanishes; once the cell temperature rises high enough to trigger the abusive reactions, the two source terms (Q_1, Q_2) coexist in Eq. (5); once the abusive reactions consume a battery material fully, the discharge/charge operation ceases and Q_1 in Eq. (5) becomes zero. In the boundary conditions of Eq. (5), h represents an equivalent heat transfer coefficient taking into consideration the convective heat release, heat radiation to the ambient, and the heat release area change as the cylindrical battery is geometrically approximated as a one-single-layer cell.

Table 1

Governing equations and boundary conditions of the ECT model [8].

Conservation equations			Boundary conditions
Charge			
Solid phase	$\frac{\partial}{\partial x}\left(\sigma^{eff}\frac{\partial}{\partial x}\varphi_s\right) - j^{Li} = 0$	(1)	$-\sigma^{eff}_{L_n}\frac{\partial\varphi_s}{\partial x}\Big|_{x=0} = \sigma^{eff}_{L_p}\frac{\partial\varphi_s}{\partial x}\Big|_{x=L} = \frac{I}{A}$
			$\frac{\partial\varphi_s}{\partial x}\Big|_{x=L_n} = \frac{\partial\varphi_s}{\partial x}\Big|_{x=L_n+L_s} = 0$
Electrolyte phase	$\frac{\partial}{\partial x}\left(\kappa^{eff}\frac{\partial}{\partial x}\varphi_e\right) + \frac{\partial}{\partial x}\left(\kappa^{eff}_D\frac{\partial}{\partial x}\ln c_e\right) + j^{Li} = 0$	(2)	$\frac{\partial\varphi_e}{\partial x}\Big|_{x=\delta} = \frac{\partial\varphi_e}{\partial x}\Big|_{x=L-\delta} = 0$
Species			
Electrolyte phase	$\frac{\partial(\varepsilon_e c_e)}{\partial x} = \frac{\partial}{\partial x}\left(D^{eff}_e\frac{\partial}{\partial x}c_e\right) + \frac{1-t^0_+}{F}j^{Li}$	(3)	$\frac{\partial c_e}{\partial x}\Big|_{x=\delta} = \frac{\partial c_e}{\partial x}\Big|_{x=L-\delta} = 0$
Solid phase	$\frac{\partial c_s}{\partial t} = \frac{D_s}{r^2}\frac{\partial}{\partial r}\left(r^2\frac{\partial c_s}{\partial r}\right)$	(4)	$\frac{\partial c_s}{\partial r}\Big|_{r=0} = 0,\ -\alpha_s F D_s\frac{\partial c_s}{\partial r}\Big|_{r=R_s} = j^{Li}(t)$
Heat	$\rho c_p\frac{\partial T}{\partial t} = \nabla\cdot\lambda\nabla T + Q_1 + Q_2$	(5)	$-\lambda\frac{\partial T}{\partial x}\Big|_{x=0} = h(T_{amb} - T),\ \frac{\partial T}{\partial x}\Big|_{x=L} = 0$
	$Q_1 = q_{ir} + q_o + q_i + q_{re} + q_c$		
	$q_{ir} = j^{Li}(\varphi_s - \varphi_e - U),\ q_o = \sigma^{eff}\nabla\varphi_s\nabla\varphi_s + \kappa^{eff}\nabla\varphi_e\nabla\varphi_e$		
	$q_i = \kappa^{eff}_D\nabla\ln c_e\nabla\varphi_e,\ q_{re} = j^{Li}\left(T\frac{\partial U}{\partial T}\right),\ q_c = \frac{I^2 R_c}{Av}$		

To quantify the electrochemical reaction rates of Li$^+$ insertion and extraction reactions in charge/discharge process, Butler-Volmer equation is considered, which is given as:

$$j^{Li} = a_s i_0\left[\exp\left(\frac{a_a F}{RT}\eta\right) - \exp\left(\frac{-a_c F}{RT}\eta\right)\right] \tag{6}$$

The ionic diffusional conductivity, κ^{eff}_D, is determined by using the concentrated solution theory, namely:

$$\kappa^{eff}_D = \frac{2R\kappa^{eff}}{F}(t^0_+ - 1)\left(1 + \frac{d\ln f_\pm}{d\ln c_e}\right) \tag{7}$$

where $f_\pm$ is the mean molar activity coefficient of the electrolyte.

2.1.2. Thermal model of battery material abusive reactions

Thermal behavior of the battery during thermal abuse process is governed by the energy conservation equation, Eq. (5). The model for the battery abusive reactions used in the present work follows the work of Kim et al. [29] and Hatchard et al. [30]. Four battery material exothermic reactions are considered, which include the decomposition reaction of solid-electrolyte interface (SEI), the reaction between the negative electrode active material and the solvent in electrolyte, the reaction between the positive electrode active material and the solvent in electrolyte, and the decomposition reaction of electrolyte; Table 2 tabulates the mathematical description of these four exothermic reactions.

The occurrence of a certain exothermic reaction depends primarily on the local cell temperature; once the cell temperature is raised higher than a threshold value, the reaction will occur. SEI film is commonly formed in anode and is electronically insulated but ionically conductive; it is metastable and decomposes exothermically at 90–120 °C[31]. The reaction of intercalated lithium with

Table 2

Thermal abuse reaction model [29,30].

Governing Equation	$\rho c_p\frac{\partial T}{\partial t} = \nabla\cdot\lambda\nabla T + Q_1 + Q_2$　(5)
Heat generation source	$Q_2 = q_{sei} + q_{ne} + q_{pe} + q_{ele}$
SEI decomposition reaction	$q_{sei} = H_{sei}W_c R_{sei},\ R_{sei}(T,c_{sei}) = A_{sei}\exp\left[-\frac{E_{a,sei}}{RT}\right]c^{m_{sei}}_{sei},$
	$\frac{dc_{sei}}{dt} = -R_{sei}$
Negative-solvent reaction	$q_{ne} = H_{ne}W_c R_{ne},$
	$R_{ne}(T,c_e,c_{neg},t_{sei}) = A_{ne}\exp\left[-\frac{t_{sei}}{t_{sei0}}\right]c^{m_{ne,n}}_{neg}\exp\left[-\frac{E_{a,ne}}{RT}\right]$
	$\frac{dt_{sei}}{dt} = R_{ne},\ \frac{dc_{neg}}{dt} = -R_{ne}$
NCM decomposition and/or Positive-solvent reaction	$q_{pe} = H_{pe}W_p R_{pe},$
	$R_{pe}(T,\alpha,c_{ele}) = A_{pe}\alpha^{m_{pe,p1}}(1-\alpha)^{m_{pe,p2}}\exp\left[-\frac{E_{a,pe}}{RT}\right],$
	$\frac{d\alpha}{dt} = R_{pe}$
Electrolyte decomposition reaction	$q_{ele} = H_e W_e R_e,\ R_e(T,c_{ele}) = A_e\exp\left[-\frac{E_{a,e}}{RT}\right]c^{m_e}_{ele},$
	$\frac{dc_{ele}}{dt} = -R_e$

the solvent of electrolyte takes place if negative electrode loses the protection of the SEI layer; its onset temperature is above 120 °C. The NCM in the positive electrode may decompose directly to release oxygen and/or react with the electrolyte solvent at higher temperatures. The electrolyte decomposes exothermically at higher temperatures (>200 °C) in the two electrodes and separator [22]. The four exothermic reactions contribute to the source term Q_2 in Eq. (5).

2.2. Model parameters

The electrolyte phase ionic conductivity κ is determined in terms of its composition. For 1.2 M LiPF$_6$ in a 2:1 vol ratio mixture of ethylene carbonate (EC) and dimethyl carbonate (DMC), κ is calculated by using the following expression [32]:

$$\kappa = 4.1253\times10^{-4} + 5.007\times10^{-3}c_e - 4.7212\times10^{-3}c^2_e$$
$$+ 1.5094\times10^{-3}c^3_e - 1.6018\times10^{-4}c^4_e \tag{8}$$

The open circuit potential (OCP) is a function of the local state of charge (SOC) or depth of discharge (DOD), and temperature. In this work, the experimental OCP data of graphite (Li$_m$C$_6$) anode and NCM (Li$_n$Ni$_{1/3}$Mn$_{1/3}$Co$_{1/3}$O$_2$) cathode are taken from [33] and [34], respectively.

Graphite anode:

$$U_{anode} = 0.1493 + 0.8493e^{-61.79m} + 0.3824e^{-665.8m} - e^{39.42m-41.92}$$
$$- 0.0313\arctan(25.59m - 4.099)$$
$$- 0.009434\arctan(32.49m - 15.74)\quad(0\leqslant m\leqslant 1) \tag{9}$$

where $m = c_{s,an}/c_{s,max,an}$.

NCM cathode:

$$U_{cathode} = -10.72n^4 + 23.88n^3 - 16.77n^2 + 2.595n + 4.563$$
$$(0.3\leqslant n\leqslant 1) \tag{10}$$

where $n = c_{s,ca}/c_{s,max,ca}$.

The temperature-dependence of parameters concerning physicochemical properties is estimated by the Arrhenius equation, as follows:

$$\Phi = \Phi_{ref}\exp\left[\frac{E_{act,\Phi}}{R}\left(\frac{1}{T_{ref}} - \frac{1}{T}\right)\right] \tag{11}$$

where Φ represents a general variable, which may be the Li-ion diffusion coefficient in electrolyte, lithium diffusivity in solid active material, ionic conductivity of electrolyte, or exchange current density.

Main model parameters including the geometrical parameters of the battery are summarized in Table 3.

For the thermal model of battery abusive reactions, physicochemical and kinetic parameters are given in Table 4.

Table 3
Model parameters for NMC lithium-ion battery ECT model [13]

Parameters	Anode	Separator	Cathode
Thickness, L (cm)	40×10^{-4}	25×10^{-4}	35×10^{-4}
Thermal conductivity, λ (W m^{-1} K^{-1}) [35]	0.4	0.5	0.4
Porosity, ε	0.59	0.42	0.54
Particle radius, r (μ m)	5	N/A	5
Maximum Li$^+$ concentration in solid $c_{s,max}$ (mol m^{-3}) [35]	31000	N/A	51800
Initial electrolyte concentration, c_e (mol cm^{-3})	1.2×10^{-3}	1.2×10^{-3}	1.2×10^{-3}
Reference exchange current density (A m^{-2}) [36]	36	N/A	26
Solid phase electronic conductivity, σ (S m^{-1})[36]	1.0	N/A	0.1
Li$^+$ diffusion coefficient in solid, D_s (m^2 s^{-1})	2.55×10^{-10} (1.5-x)$^{3.5}$where x denotes SOC		2.0×10^{-10}
Li$^+$ diffusion coefficient in electrolyte, D_e (m^2 s^{-1})	1.5×10^{-10}	1.5×10^{-10}	1.5×10^{-10}
Activation Energy for Li diffusivity, E_{act}^{De} (J mol^{-1})	10,000	N/A	10,000
Activation energy for exchange current density, $E_{act}^{i_0}$ (J mol^{-1})	30,000	N/A	30,000
Activation energy for solid phase Li diffusion coefficient, $E_{act}^{D_s}$ (J mol^{-1})	50,000	N/A	25,000
Bruggeman exponent [36]	1.5	1.5	1.5
Anodic/Cathodic transfer coefficient, α_a, α_c [36]	0.5	N/A	0.5
Current collector contact resistance, R_c (Ω m^2), estimated	0.003		
Transference number, t_+^0 [36]	0.363		
Faraday's constant, F (C mol^{-1})	96487.0		
Reference temperature (K)	298.15		

Table 4
Physical and kinetic parameters for abusive reactions [29,37,38]

Reaction heat/J kg^{-1}				Frequency factor/s^{-1}				Activation energy/J mol^{-1}			
H_{sei}	H_{ne}	H_{pe}	H_{ele}	A_{sei}	A_{ne}	A_{pe}	A_e	$E_{a,sei}$	$E_{a,ne}$	$E_{a,pe}$	$E_{a,e}$
2.57 E5	1.714 E6	7.9 E5	1.55 E5	2.25 E15	2.5 E13	2.55 E14	5.14 E25	1.3508 E5	1.3508 E5	1.5888 E5	2.74 E5

Initial dimensionless content					Reaction order					Material content/kg m^{-3}		
c_{sei0}	c_{neg0}	α_0	c_{ele0}	t_{sei0}	m_{sei}	$m_{ne,n}$	$m_{pe,p1}$	$m_{pe,p2}$	m_e	W_c	W_p	W_e
0.15	0.75	0.04	1	0.033	1	1	1	1	1	1.39E3	1.5E3	5E2

2.3. Numerical procedure

The set of Eqs. (1)–(5) with the specified boundary conditions (Table 1) and initial conditions is solved for the five unknowns: φ_s, φ_e, c_e, c_s, and T. Eq. (5) is solved by itself once battery discharge/charge process is completed or ceases due to the full consumption of a battery material (or materials) by the abusive reactions. All these equations are solved in the commercial computational fluid dynamics (CFD) flow solver, Fluent®, which is based on the finite volume approximation. By customizing its User Defined Functions (UDFs), various source terms and physicochemical properties are implemented. The first order upwind differencing scheme is used to discretize the spatial-derivative term and a fully implicit scheme is used to discretize the transient term.

The 18650 battery is geometrically approximated by an unrolled single layer cell. The simulation is actually in one-dimension perpendicular to the electrode plane. The numerical elements are hexahedral and local mesh refinement procedures were elaborately performed to ensure sufficiently fine mesh in the fast heat generation/release regions. The numerical elements have volume about 9.7×10^{-10} m^3 to 6.5×10^{-8} m^3 and the total number of numerical meshes is about 1300. Grid-independence tests were conducted to guarantee the employed mesh gives calculation results of adequate accuracy.

3. Results and discussion

3.1. Experimental validation of ECT model

Commercial 1.5 Ah 18650 LIBs with NCM cathode were selected for the experimental measurements. A battery test station (BT

2000, Arbin Instruments, USA) is employed to control and monitor the battery charge and discharge operations. The room temperature is 25 °C air-conditioned.

For the purpose of the ECT model validation, we compare the model-predicted cell voltage and temperature curves with the experimental data. The model-predicted cell voltage is determined by the following relation:

$$V = \varphi_s|_{x=L} - \varphi_s|_{x=0} \pm \frac{R_c}{A} I \qquad (12)$$

where R_c represents the total contact-resistance including the contact-resistance between the current collector and electrode, and the electric resistance of the SEI layers. The third term on the right-hand side of Eq. (12) takes the negative sign for discharge operations and the positive sign for charge operations.

The battery is charged or discharged at different C-rates, namely: 1C, 3C, 5C or 8C. Normally, to fully charge the battery, it is charged via constant current to 4.2 V and then this voltage value is kept until the charging current goes down to 0.01 A (CCCV mode); for most cases considered in this study, only the constant current charge phase is simulated. The simulation of constant current discharge processes will be terminated once the cell voltage drops to 2.8 V. The simulated voltage curves are compared with those determined experimentally in Fig. 2, and it can be observed that they are in good agreement. Along with the increase of charge/discharge rate, the total charged/discharged cell capacity presents higher deviation from the nominal value (1.5 Ah). This deviation is caused by the ineffectiveness due to the EC reactions, and/or the limited multi transport processes occurring in battery during charge/discharge operations [13,39]. Overall, the model predictions are consistent with the measurements in terms of trend and agreement.
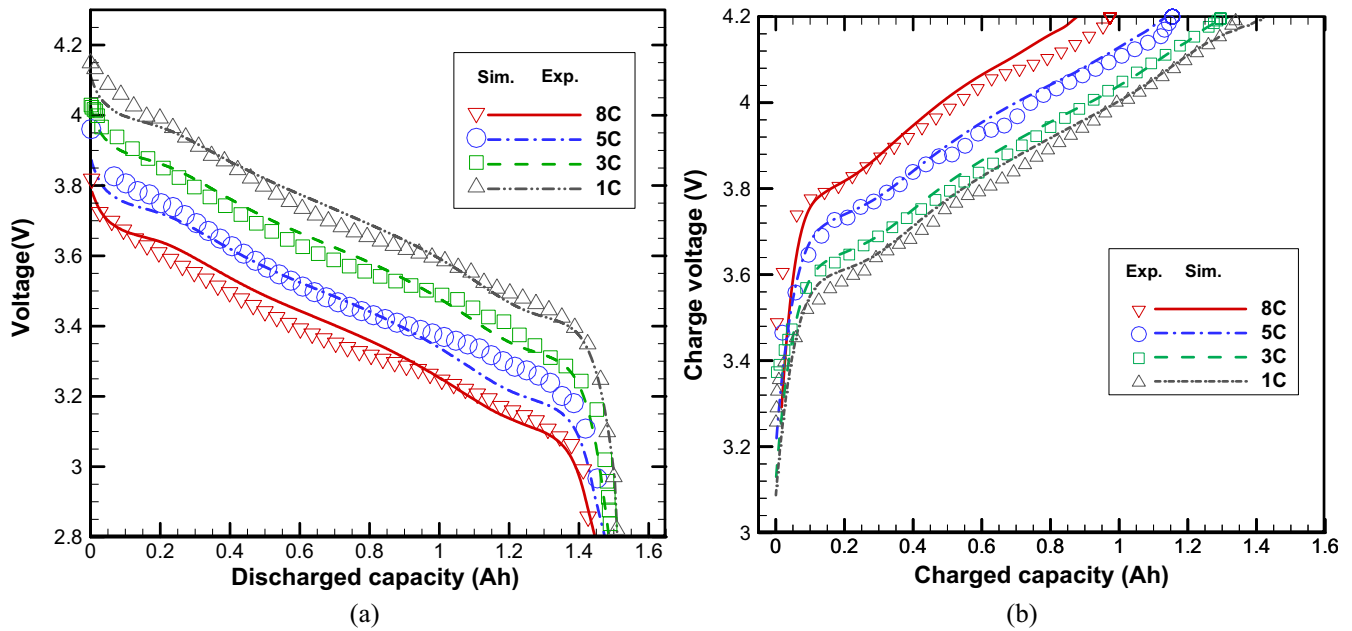
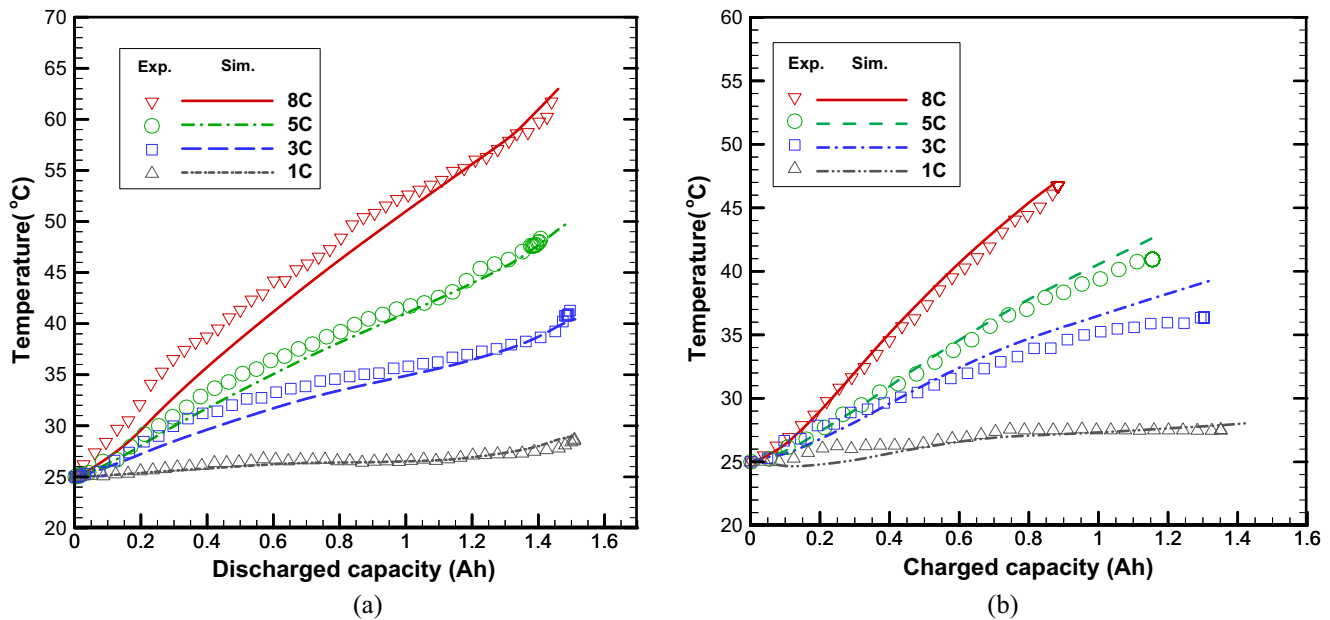**Fig. 2.** Comparison of experimental and simulated cell voltages: (a) discharge and (b) charge process.

Fig. 3. Comparison of experimental and simulated cell temperatures: (a) Discharge and (b) Charge process. (The simulation considers h = 0.53 W m^{-2} K^{-1}, corresponding to a convective heat transfer coefficient of approximately 14 W m^{-2} K^{-1} in reality.)

Fig. 3 compares simulated and experimental cell temperatures for 1C, 3C, 5C, and 8C charge and discharge processes. The temperature monitoring point is set at the center of the cell cathode outer surface. Since the simulated single layer cell is not the real cylinder-spiral battery, precisely specifying the convective heat transfer coefficient in the numerical model is very difficult. Therefore, a constant equivalent convective heat transfer coefficient (h) is estimated to achieve a good match between the simulated and experimental results; the value obtained in this way for the equivalent heat transfer coefficient (h) is 0.53 W m^{-2} K^{-1}, which yields a convective heat transfer coefficient of approximately 14 W m^{-2} K^{-1}, a value which is within the range for air natural convection [40].

It can be noted in Fig. 3 that an increase in the discharge/charge rate leads to higher cell temperature rise after the discharge/charge

operation; the cell temperature increase for the 1C, 3C, 5C, and 8C discharge process are 4 °C, 15 °C, 22 °C and 38 °C, respectively; in general, the charge process has smaller cell temperature increase than that for the discharge process with the same C-rate. For all the eight cases, the simulated cell temperatures match well the experimental results. It is worth mentioning that the cell temperature during 1C charge or discharge process sometimes is below the ambient temperature (25 °C), which may be due to a small amount of heat generated in the 1C charge/discharge process such that the negative heat sources, such as the reversible entropy heat (i.e. q_{re} in Eq. (5)), dominates the thermal behavior of the battery during this time period.

The above comparisons between simulated and experimental results fully validate the reliability of the ECT model. For dis-

charge/charge operations that have very high C-rate (>8C) and may cause thermal runaway, we will systematically analyze the thermal behavior of battery in the following sub-sections.

3.2. Very high C-rate charge and discharge with adiabatic thermal condition

It is obvious that cell temperature increases remarkably when current is tapped at high C-rate. Once we increase the current in the discharge/charge process, limited cell capacity is discharged/charged due to the early occurrence of the cut-off voltage, as shown in Figs. 2(b) and 3(b). As is well-known, LIBs perform better within a specific voltage range, for the NCM battery being considered in this study, the cut-off voltage of charge and discharge process is 4.2 V and 2.8 V, respectively.

The simulated battery temperature evolution curves during the discharge process for different C-rates: 11C, 13C and 15C are reported in Fig. 4(a). Initially, it can be easily noticed that the three cases differ in their temperature responses under the imposed C-rates. For the 13C and 15C cases, the cell temperature responds quickly upon discharging and steadily increases after a specific turning point (190 s for the 15C case and 246 s for the 13C case), eventually rises steeply to a very high value; for the 11C case, the apparent increase of cell temperature ceases after a turning point, 298 s. The just-mentioned turning points indicate the battery discharge process is over or terminated; they are annotated in Fig. 4(a) and (b).

From the time points annotated in Fig. 4(a) and (b), we can easily calculate the discharged capacity ratios are 79.2%, 88.8%, and 91.1% respectively for the three discharge cases: 15C, 13C, and 11C. Fang et al. [13] reported experimental and numerical studies on a 1.2 Ah NMC cell during 1C∼10C discharge processes. Under effective thermal management conditions, the discharge capacity for the 10C discharge process was about 1.1 Ah, approximately 91.6% of the total stored electricity was discharged. Therefore, the simulated discharge property of the NMC cell, shown in Fig. 4(a) and (b), should be reasonable.

For the 13C and 15C cases, discharge processes terminate after 246 s and 190 s, respectively. For the 15C case, the temperature increase rate is higher, but the cell temperature of the turning point is approximately the same (at about 150 °C) as that for the 13C case, due to the earlier termination of the 15C discharge process. This high cell temperature will undoubtedly yield thermal abuse of the cell material; four related thermal abuse reaction curves, which describe the reaction degree with time, are reported in Fig. 4(c)–(f) to further clarify the battery performance.

For the 15C case, the inset in Fig. 4(a) shows how the SEI film decomposition reaction proceeds with time and temperature. By inspection of Fig. 4(c)–(f) and (a) in combination of the original simulation data, it can be noticed that the SEI film decomposition reaction and negative-solvent reaction come into play during battery discharge process at 100 s (92 °C cell temperature) and 160 s (132 °C), respectively. As time progresses, the battery discharge process stops at 190 s, from this time point, the EC reaction ceases and does not contribute heat generation anymore, and heat is generated from battery material abuse reactions. SEI film runs out later at 250 s (169 °C) and the positive-solvent reaction rises at 470 s (202 °C), at this time point, heat from reactions of both electrodes with the solvent lead to further cell overheat and to the onset of the fourth abuse reaction –electrolyte decomposition reaction at 500 s (207 °C). Finally, the cell temperature climbs to ∼420 °C and the battery may lose its physical integrity due to the accumulated heat from excessive abuse reactions. It should be noted that the thermal runaway starts at a temperature close to 260 °C, as it was experimentally determined [41]; this result further validates the proposed computational model. For the three dimensionless parameters: concentration of electrolyte (c_{ele}) in the electrolyte decomposition reaction, degree of conversion of positive electrode (α) in the positive-solvent reaction, and the dimensionless amount of lithium within the carbon (c_{neg}), the evolution curves shown in Fig. 4(d)–(f) imply that the corresponding battery materials are entirely exhausted by the abuse reactions.

Similar to the 15C case, in the 13C case the cell overheats after discharge ending time, and the four thermal abuse reactions take place in succession at 145 s, 230 s, 600 s, and 625 s, respectively. It is no surprise that the 13C case ultimately goes into thermal runaway due to reaction heat from the abuse reactions.

For the 11C case, the battery discharge ends at 298 s. During discharge, the cell temperature rises to 125 °C and exceeds the onset temperature of the SEI film decomposition reaction, 92 °C, at 235 s. There is only a slight cell temperature increase after discharge and the temperature remains almost constant though the cell under the adiabatic thermal condition; therefore, for this case, due to limited cell temperature excursion, there is no occurrence of other thermal abuse reactions and thus no thermal runaway is observed.

It should be reiterated that there is a safety issue related to the potential thermal runaway during the battery discharge process; this event can be prevented in a time frame of ∼400–600 s for 13C to 15C case involving the 1.5 Ah NCM cell. Moreover, LIBs practical protective strategies, like the positive temperature coefficient (PTC, works at about 150 °C) thermistor, usually keep the battery from overheating by limiting the discharge current; however, these passive strategies may prove to be ineffective for the 13C to 15C discharge in adverse heat release conditions. To a great extent, it can be stated that when the accumulated heat in a cell is not sufficient to induce additional abuse reactions in the high temperature segment, the cell temperature will decrease and no thermal runaway will occur, as the 11C discharge process exemplifies this particular situation. However, battery thermal runaway is inevitable, when NCM cell is subjected to extensive negative-solvent abuse reaction yielding battery temperatures greater than or equal to 150 °C. Therefore, adequate heat release capability or effective and active thermal control may be the key to preventing thermal runaway of LIBs.

The model prediction of cell voltage profiles of three discharge cases, 11C, 13C, and 15C are reported in Fig. 4(b). The simulated initial voltages of the cell upon discharge are 3.65 V, 3.52 V, and 3.42 V for the 11C, 13C, and 15C discharge case, respectively. Along with the increase of discharge rate, the discharged capacity decreases to 1.19 Ah at the end of 15C discharge process. >20% of the cell capacity cannot be discharged by the constant current mode for the 15C case. All cell voltage results presume the high cell temperature (about 120 °C) does not interfere with the battery discharge process – in fact, most LIBs can still have a current output close to this temperature. Fig. 4 also reveals that the 15C case of the three cases studied is the one presenting the highest safety risk; in its discharge process, the cell reaches the highest temperature with ∼80% of the cell capacity discharged. For this reason, the thermal behavior of the battery discharge with 15C-rate will be further discussed in the next section to explore the effects of heat release condition.

Fig. 4(c)–(f) present the time-development of the four exothermic reactions for 11C, 13C and 15C discharge cases. The analysis of the four reaction degree parameters (c_{sei}, c_{neg}, α, c_{ele}) in LiCoO$_2$ cells during oven tests is available in [42].

It is interesting that the battery discharge processes with very high C-rate seemingly do not suffer explicit performance-limitations due to the species transport inside the battery, and most of the stored electricity can be output. The 15C discharge case is particularly analyzed with the characteristic parameter analysis method proposed in [39]. In [39], three parameters were defined to
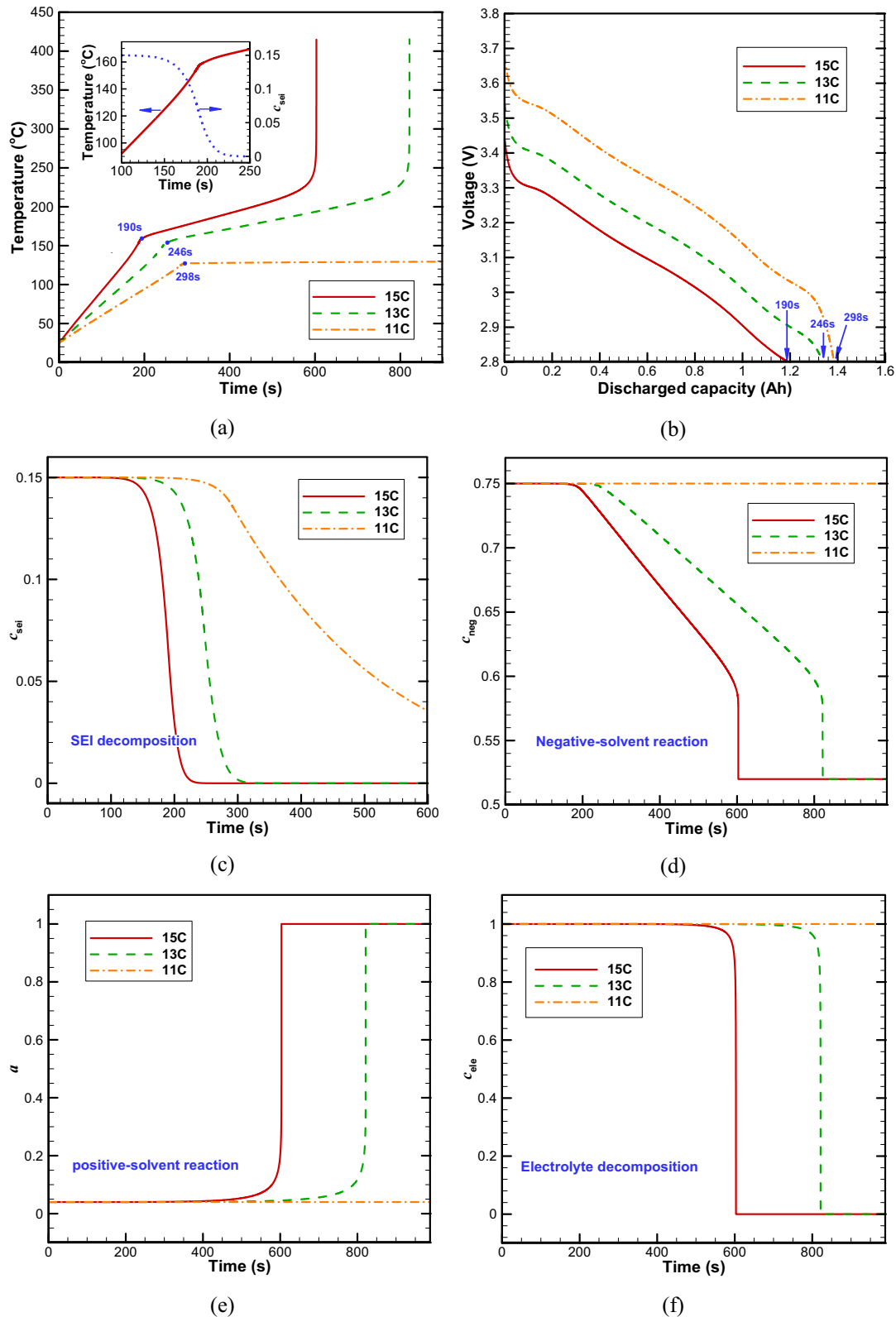
Fig. 4. Simulation results for battery discharge processes of very high C-rate: (a) cell surface temperature, (b) voltage during the discharge process; and reaction degree of the exothermic reactions: (c) SEI decomposition, (d) negative-solvent reaction, (e) positive-solvent reaction, (f) electrolyte decomposition reaction.

characterize the species transport processes, i.e. t_e, t_s and t_c, which respectively represent the characteristic time of the Li-ion transport rate in the electrolyte (t_e), the characteristic time describing the lithium diffusion process in the solid active materials (t_s),

and the characteristic time indicating the local Li-ion depletion rate in electrolyte at the electrolyte/electrode interface due to the EC reaction (t_c). Normally, a battery will not suffer any performance-limitations caused by the species transport processes

so long as the three characteristic time parameters are on the same order of magnitude; the performance-limitation of batteries at (very) high-rate operations is essentially due to the very fast local depletion of Li-ions in electrolyte at the electrolyte/electrode interface. The three characteristic times for the 15C case are calculated and tabulated in Table 5.

The data in Table 5 reveal that the t_e-s and t_s-s in anode and cathode are always larger than the corresponding t_c-s in the whole discharge process; however, the three characteristic times are generally within the same order of magnitude especially in the middle and late stages of the discharge process, which means the Li-ions (or lithium) consumed or generated at the electrolyte and electrode interface can be supplied or transported away in time. Therefore, the battery does not show evident performance-limitation during the 15C discharge operation.

Fig. 5(a) reports the temperature evolution of the charge processes with 12C, 14C, 16C, and 18C charge rate. It can be observed that the cell temperature rise is dramatically reduced with the increase of charge rate, and the charge processes for 12C, 14C, 16C, and 18C terminate at 109 s, 62 s, 48 s and 9 s, respectively. In these charge cases, the highest temperature 81 °C occurs for the terminal time of the 12C charge case. Therefore, based on the triggering temperature of the abuse reactions, no thermal abuse reaction occurs for these four charge processes.

Fig. 5(b) presents the voltage evolution for the charge cases mentioned above; with the increase of charge rate, cell voltage

curves become increasingly steep and, consequently less capacity is charged into the battery, in particular for the 18C charge process, where the input energy brought into the battery is only 0.06 Ah. In general, less than 0.6 Ah cell capacity is charged into the battery with a very high charge rate above 12C.

The occurrence of early-coming cut-off voltage and limited charged capacity for very high C-rate charge cases can only be partially ascribed to the limited multi transport inside the battery [39] according to the above-detailed characteristic parameter analysis in relation to the 15C discharge case. The main reason causing the early-coming cut-off voltage may be the large ohmic loss in the very high C-rate charge operations.

Figs. 4 and 5 collectively indicate that the goal of NCM battery higher current output and fast charging strategy cannot be easily realized by merely enhancing the C-rate of the charge/discharge operation. The reason is that cell temperature and cut-off voltage synergistically influence the characteristics of the battery charge/discharge operations.

3.3. Very high C-rate discharge with different heat release conditions

Favorable heat releasing conditions are required to avoid overheat in LIBs and, eventually, thermal abuse/thermal runaway, in particular for very high C-rate discharge processes. For their importance, different heat release conditions for the 15C discharging

Table 5
The calculated characteristic times for the 15C discharge process.

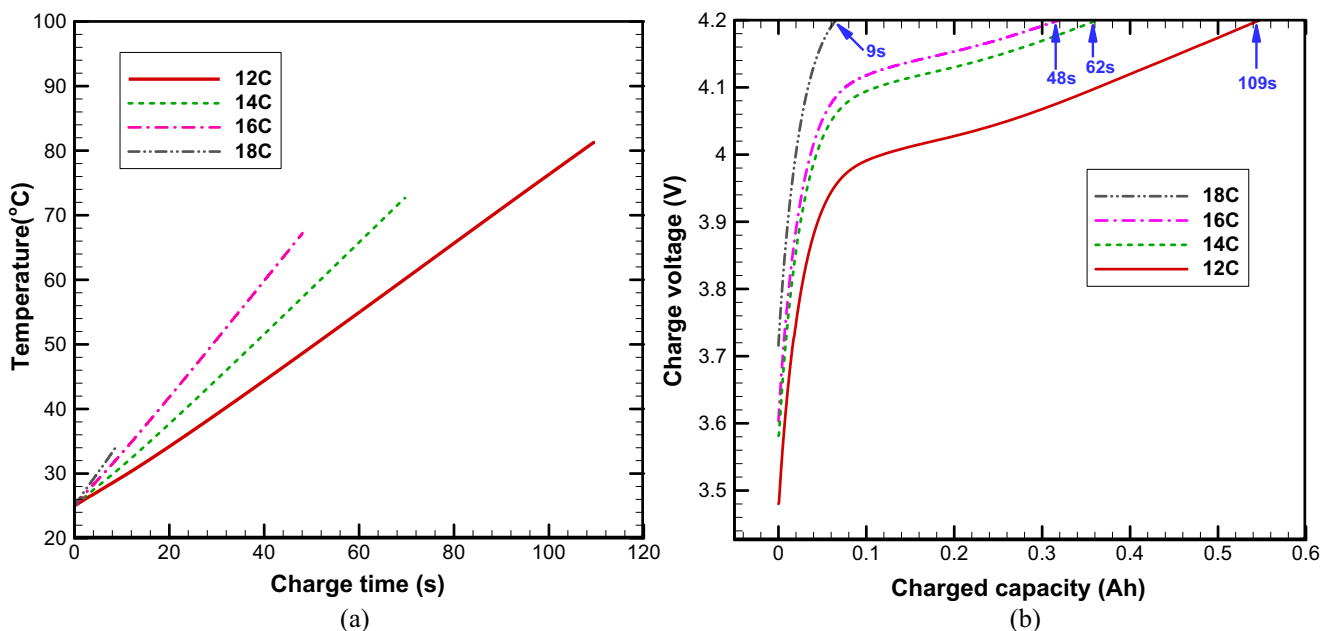| Time instant (s)	t_e (s)	t_s (s)		t_c (s)	
		Anode	Cathode	Anode	Cathode
0.5	35.6–36.7	1177.0–1219.1	138.9–150.0	18.8–48.1	11.7–16.6
5		687.6–1076.7		4.7–33.8	9.5–14.1
10		415.0–1000.5		5.2–54.1	9.4–11.5
50		80.6–524.7		8.14–21.9	8.4–11.1
100		53.5–193.3		10.4–24.5	8.0–10.9
130		49.1–95.7		8.9–33.7	7.8–10.8
150		45.8–63.7		6.7–33.4	7.8–10.7
170		39.1–48.78		9.6–18.2	7.8–10.8
190		33.7–41.4		23.6–33.1	7.2–11.6

Fig. 5. Evolution of (a) cell temperature and (b) voltage during the charge processes of very high C-rate.

case, which has high possibility of cell thermal runaway will be discussed in this section.

Battery temperature response to different equivalent heat transfer coefficients (h) during and after 15C discharge operation is reported in Fig. 6(a). It can be seen that batteries ultimately go to thermal runaway with high temperature when equivalent heat transfer coefficient equals zero and 0.05 W m^{-2} K^{-1}, and no thermal runaway happens in other cases (h = 0.25, 0.53, 1.10, and 2.20 W m^{-2} K^{-1}). For the cases with battery thermal runaway, the LIBs out-of-control occurrence starts at 603 s and 773 s for the adiabatic condition (h = 0 W m^{-2} K^{-1}) and h = 0.05 W m^{-2} K^{-1}, respectively. The latter case releases part of battery inner heat during and after discharge, which leads to cell temperature slightly lower than that of the adiabatic case, which further slows down the thermal abuse reactions rate; however, the limited heat dissipation is not sufficient to avoid the eventual thermal runaway. Therefore, enhancing the heat release is an essential way of conducting an effective thermal management of the battery. As expected, when h takes the value as 0.25 W m^{-2} K^{-1} and 0.53 W m^{-2} K^{-1}, cell temperature decreases slowly after the ending time point of discharge (~190 s); when h is 1.1 W m^{-2} K^{-1}, cell temperature decreases quickly after discharge and no exothermic reactions are initiated except for the SEI decomposition in anode; cell temperature is remarkably reduced and almost no abuse reactions appear when h is equal to 2.2 W m^{-2} K^{-1}, which is equivalent to a real convective heat transfer coefficient ~61 W m^{-2} K^{-1}.

Fig. 6(b) presents the time evolution of the cell voltage during and after 15C discharge operation with different values of h. Cell voltages for the different cases analyzed drop from ~3.44 V to 2.8 V. The six voltage profiles present a very similar trace; the locally magnified inset in Fig. 6(b) clearly shows there are some differences though minimal. For the battery discharge processes, the highest and the lowest cell voltage output correspond to the adiabatic condition and to the highest h (2.2 W m^{-2} K^{-1}), respectively; however, the difference between them is relatively small with a value of approximately 10 mV.

For a practical battery pack consisting of many individual cells, the cells at different locations may have differing heat release conditions. The innermost cell generally has the most adverse heat

release condition, or even adiabatic thermal condition, and is thus more vulnerable to thermal runaway. Thermal management of a battery pack needs to adequately consider these factors.

3.4. A potential charging fault of very high C-rate charge process

Given the fact that fully recharging EVs with Level II-240 V charging station takes from 6 to 8 h [43], this charging time is rather long and it does not meet the requirements of many practical situations. In Section 3.2, the cell temperature and voltage were examined during the charge process with very high C-rate (above 12C), and it was observed that only 0.08–0.54 Ah capacity is charged into the battery when the current rate decreases from 18C to 12C.

Hence, high or very high C-rate fast charging will become the possible strategy to overcome the extended charging time issue; however, this strategy should take into account the eventual degradation of the battery. As previously stated, very limited capacity is charged into the cell with very high charge rate (Fig. 5(b)) and probably more time will be wasted in fully charging it by CCCV mode, which may jeopardize this possible charge strategy. In our view, a wise choice may be a balance between charged capacity and charge time, so the 12C charge would become the primary choice in the fast charging strategy. Moreover, a major concern of fast charging the battery is a possible control fault of the cut-off voltage (4.2 V); under these conditions, the battery is continuously charged at a constant current. In this section, this fault event is further explored.

Fig. 7 reports the characteristics of the voltage and temperature curves for an uncontrolled 12C charge battery under adiabatic thermal condition. As suggested in Fig. 5, proper measures should be taken to cease charge at 109 s reaching the cut-off voltage; this corresponding situation is marked out with two highlight points in Fig. 7(a): 4.2 V on the voltage profile and 81 °C on the temperature profile. Beyond these two points, the battery is subjected to no protective measures and consequently, leading to possible incidents. As this control fault progresses, four thermal abuse reactions are activated, which can be observed in terms of the reaction degree with charge time in Fig. 7. The SEI decomposition reaction and
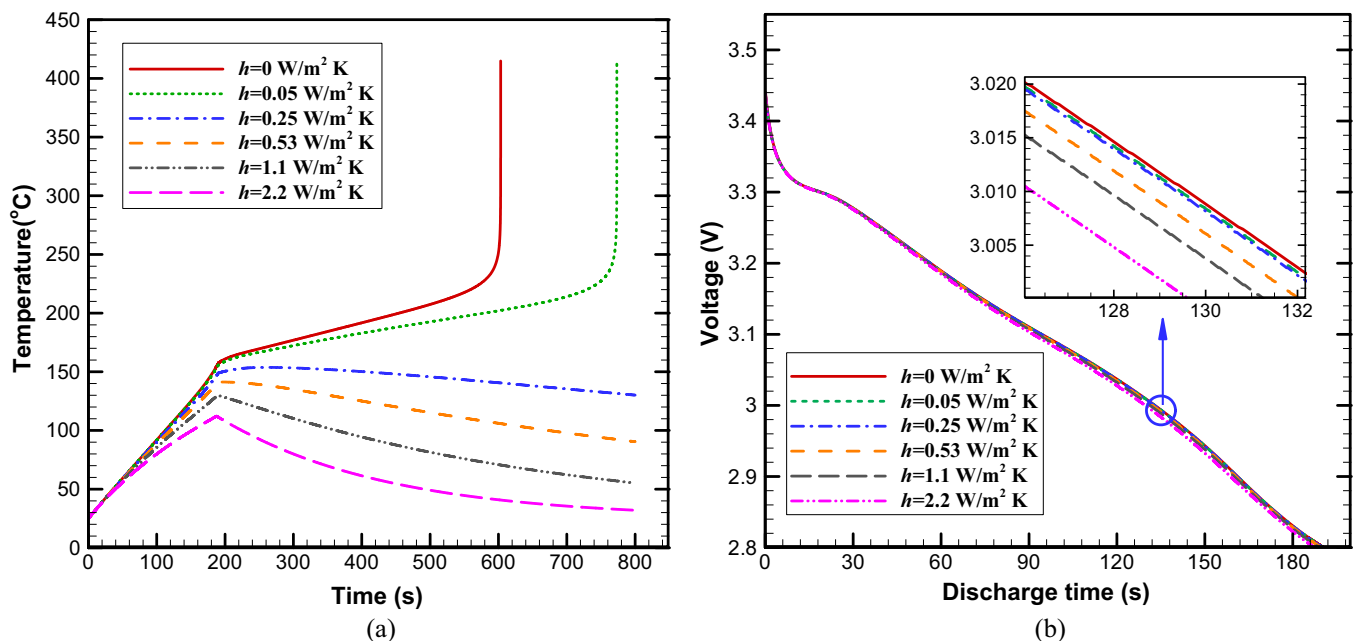

Fig. 6. Profiles of cell surface temperature and voltage in 15C discharge case with various values of *h*.
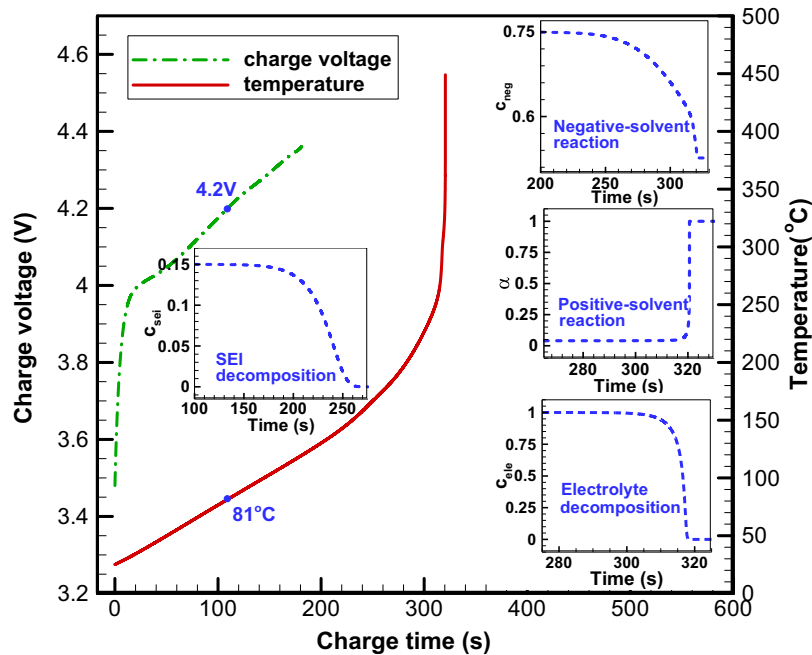
Fig. 7. Characteristics of the voltage and temperature of for an uncontrolled 12C charge battery under adiabatic thermal condition.

negative-solvent reaction occur at 130 s (92 °C) and 210 s (132 °C), respectively, with the SEI decomposition reaction completed at 260 s (~260 °C). The positive-solvent reaction starts at 284 s (202 °C), the continuous overheat inside the cell causes the electrolyte to decompose at 288 s (207 °C). At last, battery thermal runaway occurs at 320 s.

Obviously, the situation of 12C charge battery with a faulty control is by far more dangerous than the high-C rate discharge cases; a steady stream of power input could push the cell to the threshold point of 150 °C in ~130 s, and ~80 s later leading to thermal runaway. The 15C discharge needs ~400 s for the occurrence of thermal runaway after discharge. In addition, cell charge voltage grows steadily with this faulty control. Taking into consideration the consequence of the abuse reaction, in the simulation the charge process is terminated when the cell voltage reaches 4.35 V.

4. Conclusions

It was proposed a numerical model, which has the unique feature of investigating the thermal behavior of lithium-ion batteries in its entirety from cell discharge/charge to thermal abuse/thermal runaway due to heat generation from battery material exothermic reactions. This model combines an ECT module with a thermal abuse module with the purpose of studying the dynamic response of NCM cells during and after very high C-rate charge/discharge processes. The benchmarking and validation of model was accomplished using experimental data obtained for this specific purpose.

Results indicate that there exists a safety issue related to the potential thermal runaway during the battery discharge process, and the amount of heat production from very high C-rate discharge process is enough to push the lithium-ion battery, under specific conditions, toward an eventual thermal runaway. For the 1.5 Ah 18650 NCM/Graphite cells considered, thermal runaway is always triggered after discharge if the imposed C-rate reaches 13C in an adiabatic environment, similar observation was made for the 15C discharge case under restricted heat releasing conditions (h not >0.05 W m^{-2} K^{-1}). However, no thermal runaway or even thermal abuse reactions occur during a very high C-rate charge process as

the charge operation is terminated by the early-coming of cut-off voltage. Additionally, the effect of a faulty control for the cut-off voltage on a 12C charge battery was also investigated and, interestingly, this situation was found to be far more dangerous than any other high-C rate discharge cases.

Adequate heat release capability or effective and active thermal control was found to be the key to preventing thermal runaway of LIBs. The SEI decomposition reaction and negative-solvent abuse reaction heat the battery temperature >150 °C will inevitably lead to thermal abuse in adverse heat release condition, even if the battery is equipped with some passive thermal control device (e.g. PTC). Simulation results demonstrate that the heat release condition and the C-rate value are the main parameters influencing LIB's thermal behaviors. The critical time point for thermal runaway dramatically changes by increasing the C-rate in the discharge process. For 13C and 15C discharge processes, the thermal runaway takes place between 600 s and 800 s, and for a safe discharge process with high C-rates the equivalent heat transfer coefficients should be maintained >2.2 W m^{-2} K^{-1}.

References

[1] S. Abada, G. Marlair, A. Lecocq, M. Petit, V. Sauvant-Moynot, F. Huet, Safety focused modeling of lithium-ion batteries: a review, J. Power Sources 306 (2016) 178–192, https://doi.org/10.1016/j.jpowsour.2015.11.100.

[2] A. Khandelwal, K.S. Hariharan, P. Gambhire, S.M. Kolake, T. Yeo, S. Doo, Thermally coupled moving boundary model for charge-discharge of LiFePO$_4$/C cells, J. Power Sources 279 (2015) 180–196, https://doi.org/10.1016/ j. jpowsour.2015.01.018.

[3] Y. Abdul-quadir, T. Laurila, J. Karppinen, K. Jalkanen, K. Vuorilehto, L. Skogström, M. Paulasto-kröckel, Heat generation in high power prismatic Li-

ion battery cell with LiMnNiCoO$_2$ cathode material, Int. J. Energy Res. 38 (2014) 1424–1437.

[4] S.J. Drake, M. Martin, D.A. Wetz, J.K. Ostanek, S.P. Miller, J.M. Heinzel, A. Jain, Heat generation rate measurement in a Li-ion cell at large C-rates through temperature and heat flux measurements, J. Power Sources 285 (2015) 266–273, https://doi.org/10.1016/j.jpowsour.2015.03.008.

[5] T. Grandjean, A. Barai, E. Hosseinzadeh, Y. Guo, A. Mcgordon, J. Marco, Large format lithium ion pouch cell full thermal characterisation for improved electric vehicle thermal management, J. Power Sources 359 (2017) 215–225, https://doi.org/10.1016/j.jpowsour.2017.05.016.

[6] D. Anthony, D. Wong, D. Wetz, A. Jain, Non-invasive measurement of internal temperature of a cylindrical Li-ion cell during high-rate discharge, Int. J. Heat Mass Transfer 111 (2017) 223–231, https://doi.org/10.1016/j.ijheatmasstransfer.2017.03.095.

[7] Y. Ye, L.H. Saw, Y. Shi, K. Somasundaram, A.A.O. Tay, Effect of thermal contact resistances on fast charging of large format lithium ion batteries, Electrochim. Acta 134 (2014) 327–337, https://doi.org/10.1016/j.electacta.2014.04.134.

[8] F. Jiang, P. Peng, Y. Sun, Thermal analyses of LiFePO$_4$/graphite battery discharge processes, J. Power Sources 243 (2013) 181–194, https://doi.org/10.1016/j.jpowsour.2013.05.089.

[9] V. Srinivasan, C.Y. Wang, Analysis of electrochemical and thermal behavior of li-ion cells, J. Electrochem. Soc. 150 (2003) A98, https://doi.org/10.1149/1.1526512.

[10] S.S. Madani, M. Swierczynski, S.K. Krer, The discharge behavior of lithium-ion batteries using the dual-potential multi-scale multi-dimensional (MSMD) battery model, in: 2017 Twelfth International Conference on Ecological Vehicles and Renewable Energies (EVER), Monte-Carlo, Monaco, 2017.

[11] L. Cai, R.E. White, An efficient electrochemical-thermal model for a lithium-ion cell by using the proper orthogonal decomposition method, J. Electrochem. Soc. (2010) 1188–1195, https://doi.org/10.1149/1.3486082.

[12] A. Maheshwari, M. Aneta, M. Destro, M. Santarelli, A modelling approach to understand charge discharge differences in thermal behaviour in lithium iron phosphate-graphite battery, Electrochim. Acta 243 (2017) 129–141, https://doi.org/10.1016/j.electacta.2017.05.049.

[13] W. Fang, O.J. Kwon, C.Y. Wang, Electrochemical–thermal modeling of automotive Li-ion batteries and experimental validation using a three-electrode cell, Int. J. Energy Res. 34 (2010) 107–115.

[14] Q. Sun, Q. Wang, X. Zhao, J. Sun, Z. Lin, Numerical study on lithium titanate battery thermal response under adiabatic condition, Energy Convers. Manage. 92 (2015) 184–193, https://doi.org/10.1016/j.enconman.2014.12.019.

[15] G.G. Botte, B.A. Johnson, R.E. White, J.E. Soc, L. Cell, G.G. Botte, B.A. Johnson, R.E. White, Influence of some design variables on the thermal behavior of a lithium-ion cell, J. Electrochem. Soc. 146 (1999) 914–923, https://doi.org/10.1149/1.1391700.

[16] Y. Ye, Y. Shi, N. Cai, J. Lee, X. He, Electro-thermal modeling and experimental validation for lithium ion battery, J. Power Sources 199 (2012) 227–238.

[17] M. Chen, Q. Sun, Y. Li, K. Wu, B. Liu, P. Peng, Q. Wang, P. Grid, P. Generation, A thermal runaway simulation on a lithium titanate battery and the battery module, Energies 8 (2015) 490–500, https://doi.org/10.3390/en8010490.

[18] S. Du, M. Jia, Y. Cheng, Y. Tang, H. Zhang, L. Ai, International Journal of Thermal Sciences Study on the thermal behaviors of power lithium iron phosphate (LFP) aluminum-laminated battery with different tab configurations, Int. J. Therm. Sci. 89 (2015) 327–336, https://doi.org/10.1016/j.ijthermalsci.2014.11.018.

[19] B. Kang, G. Ceder, Battery materials for ultrafast charging and discharging, Nature 457 (2009) 190–193, https://doi.org/10.1038/nature07853.

[20] J.M. Chem, X. Zhou, F. Wang, Z. Liu, Graphene modified LiFePO4 cathode materials for high power lithium ion, 2011, pp. 3353–3358. doi:10.1039/c0jm03287e.

[21] H. Quebec, J. Goodenough, Response to "Unsupported claims of ultrafast charging of li-ion batteries", J. Power Sources 194 (2009) 1021–1023, https://doi.org/10.1016/j.jpowsour.2009.05.043.

[22] C.F. Lopez, J.A. Jeevarajan, P.P. Mukherjee, Characterization of lithium-ion battery thermal abuse behavior using experimental and computational analysis, J. Electrochem. Soc. 162 (2015) A2163–A2173, https://doi.org/10.1149/2.0751510jes.

[23] P. Peng, F. Jiang, Thermal behavior analyses of stacked prismatic LiCoO$_2$ lithium-ion batteries during oven tests, Int. J. Heat Mass Transfer 88 (2015) 411–423, https://doi.org/10.1016/j.ijheatmasstransfer.2015.04.101.

[24] G. Guo, B. Long, B. Cheng, S. Zhou, P. Xu, B. Cao, Three-dimensional thermal finite element modeling of lithium-ion battery in thermal abuse application, J. Power Sources 195 (2010) 2393–2398, https://doi.org/10.1016/j.jpowsour.2009.10.090.

[25] T.D. Hatchard, Importance of heat transfer by radiation in li-ion batteries during thermal abuse, Electrochem. Solid-State Lett. 3 (1999) 305, https://doi.org/10.1149/1.1391131.

[26] K.J. Lee, K. Smith, A. Pesaran, G.H. Kim, Three dimensional thermal-, electrical-, and electrochemical-coupled model for cylindrical wound large format lithium-ion batteries, J. Power Sources 241 (2013) 20–32, https://doi.org/10.1016/j.jpowsour.2013.03.007.

[27] M. Doyle, T.F. Fuller, J. Newman, Modeling of galvanostatic charge and discharge of the lithium/polymer/insertion cell, J. Electrochem. Soc. 140 (1993) 1526–1533.

[28] T.F. Fuller, M. Doyle, J. Newman, Simulation and optimization of the dual lithium ion insertion cell, J. Electrochem. Soc. 141 (1994) 1–10.

[29] G.H. Kim, A. Pesaran, R. Spotnitz, A three-dimensional thermal abuse model for lithium-ion cells, J. Power Sources 170 (2007) 476–489, https://doi.org/10.1016/j.jpowsour.2007.04.018.

[30] T.D. Hatchard, D.D. MacNeil, a. Basu, J.R. Dahn, thermal model of cylindrical and prismatic lithium-ion cells, J. Electrochem. Soc. 148 (2001) A755, https://doi.org/10.1149/1.1377592.

[31] R. Spotnitz, J. Franklin, Abuse behavior of high-power, lithium-ion cells, J. Power Sources 113 (2003) 81–100.

[32] M. Doyle, J. Newman, A.S. Gozdz, C.N. Schmutz, J.M. Tarascon, Comparison of modeling predictions with experimental data from plastic lithium ion cells, J. Electrochem. Soc. 143 (1996) 1890–1903.

[33] M.W. Verbrugge, B.J. Koch, Electrochemical analysis of lithiated graphite anodes, J. Electrochem. Soc. 150 (2003) A374–A384.

[34] N. Yabuuchi, Y. Makimura, T. Ohzuku, Solid-state chemistry and electrochemistry of LiCo$_{1/3}$Ni$_{1/3}$Mn$_{1/3}$O$_2$ for advanced lithium-ion batteries iii. rechargeable capacity and cycleability, J. Electrochem. Soc. 154 (2007) A314–A321.

[35] W. Zhao, G. Luo, C.Y. Wang, Modeling internal shorting process in large-format li-ion cells, J. Electrochem. Soc. 162 (2015) A1352–A1364, https://doi.org/10.1149/2.1031507jes.

[36] K. Smith, C.Y. Wang, Solid-state diffusion limitations on pulse operation of a lithium ion cell for hybrid electric vehicles, J. Power Sources 161 (2006) 628–639, https://doi.org/10.1016/j.jpowsour.2006.03.050.

[37] X. Feng, X. He, M. Ouyang, L. Lu, P. Wu, C. Kulp, S. Prasser, Thermal runaway propagation model for designing a safer battery pack with 25Ah LiNi$_x$Co$_y$Mn$_z$O$_2$ large format lithium ion battery, Appl. Energy 154 (2015) 74–91, https://doi.org/10.1016/j.apenergy.2015.04.118.

[38] H. Wang, A. Tang, K. Huang, Oxygen evolution in overcharged Li$_x$Ni$_{1/3}$Co$_{1/3}$Mn$_{1/3}$O$_2$ electrode and its thermal analysis kinetics, Chin. J. Chem. 29 (2011) 1583–1588.

[39] F. Jiang, P. Peng, Elucidating the performance limitations of lithium-ion batteries due to species and charge transport through five characteristic parameters, Sci. Rep. 6 (2016) 32639, https://doi.org/10.1038/srep32639.

[40] J.P. Martin, Heat Transfer, tenth ed., McGraw-hill, New York, 2010, pp. 11–12.

[41] X. Feng, J. Sun, M. Ouyang, F. Wang, X. He, L. Lu, H. Peng, Characterization of penetration induced thermal runaway propagation process within a large format lithium ion battery module, J. Power Sources 275 (2015) 261–273, https://doi.org/10.1016/j.jpowsour.2014.11.017.

[42] P. Peng, Y. Sun, F. Jiang, Thermal analyses of LiCoO$_2$ lithium-ion battery during oven tests, Heat Mass Transfer 50 (2014) 1405–1416, https://doi.org/10.1007/s00231-014-1353-x.

[43] D. Anseán, M. González, J.C. Viera, V.M. García, C. Blanco, M. Valledor, Fast charging technique for high power lithium iron phosphate batteries: A cycle life analysis, J. Power Sources 239 (2013) 9–15, https://doi.org/10.1016/j.jpowsour.2013.03.044.